Journal of Colloid and Interface Science 659 (2024) 926–935

Contents lists available at ScienceDirect

Journal of Colloid And Interface Science

journal homepage: www.elsevier.com/locate/jcis

Regular Article

Ordered hierarchical superlattice amplifies coated-CeO_2 nanoparticles luminescence

Noemi Gallucci [a,b], Marie-Sousai Appavou [c,1], Nathan Cowieson [d], Gerardino D'Errico [a,b], Rocco Di Girolamo [a], Stefano Lettieri [e], Filomena Sica [a], Giuseppe Vitiello [b,f], Luigi Paduano [a,b,*]

[a] Department of Chemical Sciences, University of Naples Federico II, 80126 Naples, Italy,
[b] CSGI, Center for Colloid and Surface Science, 50019 Sesto Fiorentino, Italy
[c] Jülich Center for Neutron Science (JCNS) at Heinz Maier-Leibnitz Zentrum (MLZ), Forschungszentrum Jülich GmbH, Lichtenbergstr. 1, 85748 Garching, Germany,
[d] Diamond Light Source, Didcot, Oxfordshire, England, United Kingdom
[e] Department of Physics, University of Naples Federico II, Via Cupa Cintia 21, 80126 Naples, Italy,
[f] Department of Chemical, Materials and Production Engineering, University of Naples Federico II, 80125 Naples, Italy

GRAPHICAL ABSTRACT

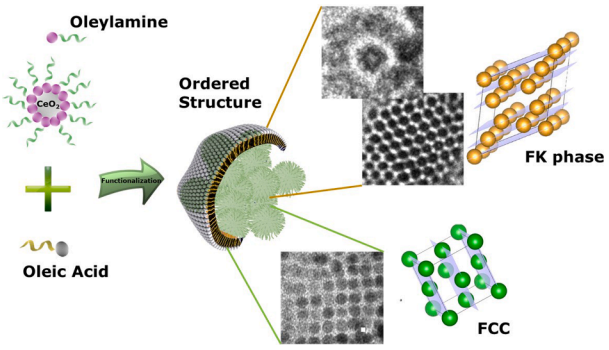

ARTICLE INFO

Keywords:
Cerium oxide
Hierarchical organization
Frank-Kasper phase
Superlattice
Photoluminescence

ABSTRACT

Achieving a controlled preparation of nanoparticle superstructures with spatially periodic arrangement, also called superlattices, is one of the most intriguing and open questions in soft matter science. The interest in such regular superlattices originates from the potentialities in tailoring the physicochemical properties of the individual constituent nanoparticles, eventually leading to emerging behaviors and/or functionalities that are not exhibited by the initial building blocks. Despite progress, it is currently difficult to obtain such ordered structures; the influence of parameters, such as size, softness, interaction potentials, and entropy, are neither fully understood yet and not sufficiently studied for 3D systems. In this work, we describe the synthesis and characterization of spatially ordered hierarchical structures of coated cerium oxide nanoparticles in water suspension prepared by a bottom-up approach. Covering the CeO_2 surface with amphiphilic molecules having chains of appropriate length makes it possible to form ordered structures in which the particles occupy well-defined positions. In the present case superlattice arrangement is accompanied by an improvement in photoluminescence

* Corresponding author at: Department of Chemical Sciences, University of Naples Federico II, 80126 Naples, Italy.
E-mail address: luigi.paduano@unina.it (L. Paduano).

[1] This work is dedicated to the memory of Marie-Sousai Appavou, a co-author of this paper, who passed away prematurely last September.

https://doi.org/10.1016/j.jcis.2024.01.029
Received 13 May 2023; Received in revised form 30 December 2023; Accepted 4 January 2024
Available online 9 January 2024

(PL) efficiency, as an increase in PL intensity of the superlattice structure of up to 400 % compared with that of randomly dispersed nanoparticles was observed. To the best of our knowledge, this is one of the first works in the literature in which the coexistence of 3D structures in solution, such as face-centered cubic (FCC) and Frank-Kasper (FK) phases, of semiconductor nanoparticles have been related to their optical properties.

1. Introduction

In recent years, the controlled clustering of inorganic nanoparticles (NPs) into defined geometric arrangements has emerged as a distinguishing feature of new soft materials with original physicochemical properties. Clusters of nanoparticles with a regular spatial arrangement are usually indicated with the term "superlattices". They can integrate the intrinsic properties of individual NPs with unique collective optical, electronic, and mechanical properties tunable by the *meso*-structure. [1–3]

The formation of ordered NP structures in solution at the nanoscale is a complex process that can be achieved by modifying interactions between ligands, possibly present on the surface, or the surface itself, and involves a balance of different forces. Among these, the main ones are van der Waals, electrostatic, lyophobic, and elastic forces between the ligands, and the solvent polarity. [2] Van der Waals forces are driven by electrical interactions induced between two or more NPs when they approach each other. [4–10] In contrast, pure electrostatic interactions occur for charged molecules present on the surface of the NPs.[11–17] Hydrophobic interactions, which occur over a long range, are due to the unfavorable interaction between the molecules that coat them and the solvent. The elastic ones arise because of the loss of configurational entropy of the ligand chains when the NPs are at very close distances. [18–21] Understanding under what conditions and how NPs spontaneously arrange themselves in regular 3D configurations is an open challenge. In general, when NP interactions are well-described by hard-sphere interparticle potentials they form compact structures like face-centered cubic (FCC), hexagonal closed-packed (HPC), or body-centered cubic (BCC) structures.[22] However, in a few cases more complex arrangements, such as Frank-Kasper or tetrahedral close packing (TCP) phases, or even quasi-crystalline structures, observed mainly in polymeric systems, have been observed.[23–27] In particular, the Frank-Kasper phase is characterized by the arrangement of particles that form a hierarchical structure at the vertices of almost regular tetrahedrons.[28]

Recently, Pansu *et al.* argued that the formation of different structures is governed by a complex combination of physicochemical parameters, including: *i*) the radius of the inorganic core r_c, *ii*) the alkyl chain length l_s, and *iii*) the minimum thickness between two neighboring NPs. The ligand-binding interaction determines the degree of order of the superlattice, the spacing between the particle nuclei, the type of lattice, and its physical properties.[22]

Thanks to their peculiar properties, NP superlattices, in which the original properties of NPs are amplified if they are arranged in an ordered structure, such as FCC, BCC, or Frank-Kasper phases, can be used in various fields: photonics, catalysis, and medicine. For example, the optical properties of NP superlattices depend noticeably on their geometry, making it possible to engineer their electric and magnetic responses over a broad range.[1,29] At present, light-matter interaction has been mainly studied for 2D systems and never for superlattices of dispersed NPs. In addition, these studies have been carried out mainly using metal nanoparticles.[30–32]

Normally, two general procedures can be followed to form a regular spatial arrangement of self-assembled clusters in suspension: *i*) a one-step "*in situ*" route in which NPs are synthesized and assembled within the same process; *ii*) a two-step approach in which the NPs are first synthesized and then the self-assembly is induced. The latter procedure has more advantages because NPs of the highest quality (in terms of size, shape, crystallinity, and polydispersity) can be used.[2] Generally, the NPs used to form an assembled cluster are synthesized through a wet chemical method, using a capping agent to control the size and shape. This organic coating allows the subsequent formation of an NP aggregate through, for example, an emulsion process.[33]

Among the various metal oxides with interesting physicochemical properties, cerium oxide (CeO_2) is particularly intriguing. Cerium is the most abundant Rare Earth element on Earth's crust and CeO_2-NPs show extraordinary properties in exerting a continuous redox cycle through a tuning of oxidation states (Ce^{3+}/Ce^{4+}). This ability together with the long luminescence lifetime of the charge carriers and high oxygen mobility allows the use of CeO_2-NPs in photocatalysis.[34,35] Semiconductor CeO_2 NPs have a wide bandgap (3.0–3.4 eV) and can act as a photocatalyst if irradiated by UV light, similarly to TiO_2 NPs, but with the advantage of longer lifetime of the charge carriers and higher oxygen mobility.[36,37] This allows to use CeO_2 NPs in bioimaging, biosensors, photocatalysis, and nanomedicine.[38,39] In recent years CeO_2-NPs have attracted great interest in the biomedical field (i.e., as anticancer, antioxidant, and antibacterial agents), due to their redox properties which can be opportunely modulated to inhibit (antioxidant action) or promote (pro-oxidant action) the oxidation processes,[40–43] showing the ability to decrease or to increase the concentration of the Reactive Oxygen Species (ROS).[44–46] Finally, CeO_2 NPs have acquired increasing attention due to their peculiar behavior that places them into the promising category of "nanozymes", which are NPs with enzyme-like features. Indeed, they show superoxide dismutase, catalase, and phosphatase mimetic activity.[44,45]

Here, we report on the procedure to obtain ordered hierarchical structures of coated CeO_2-NPs and on the effect that the regular spatial distribution produces on the optical properties of such nanoparticles. First, CeO_2-NPs coated with oleylamine (OL) used as a capping agent were synthesized. Then, the promotion of the self-aggregation by the emulsion process in the presence of oleic acid (OA) was investigated by the combination of Dynamic Light Scattering (DLS), Small-Angle X-ray Scattering (SAXS), Transmission Electron Microscopy (TEM), cryo-TEM, fluorescence and photoluminescence (PL) to correlate the supramolecular organization of coated NPs, and their regular spatial arrangement, with the fluorescence behavior. The choice of a multi-methodological approach lies in investigating the structural and morphological properties of these aggregates both in solution and as dry samples, to demonstrate that the obtainable superlattices exert good stability and emission behavior both in water as well as in the dehydrated state. The obtained aggregates (200–300 nm, referred to as *meso* structures) show a very regular spatial arrangement at the nanoscale. Structural data suggest the coexistence of face-centered cubic and hexagonal phases, possibly Frank-Kasper phases. In conjunction with the formation of ordered structures, a strong amplification of the intrinsic photoluminescence of the NPs is observed.

This work aims to contribute to the engineering development of superlattice complexes of inorganic nanoparticles showing an enhancement of the original intrinsic properties and leading, when appropriately combined, to systems with original physical properties that can be applied in different technological fields.

2. Experimental section/methods

2.1. Materials

Cerium(III) nitrate hexahydrate (>99.999 % trace metals basis purity), 1-Octadecene (90 % technical grade), oleylamine (OL, 70 %

technical grade), chloroform (≥99.5 %, contains 100–200 ppm amylenes as a stabilizer), oleic acid (OA, ≥99 % purity), and sodium oleate (NaOA, 99 % purity) were purchased from Merck (Germany) and used without further purification. All aqueous solutions were prepared using double-distilled Milli-Q water, filtered using 0.20 μm filters, with the only exception of samples for Cryo-TEM where D_2O (Merk) was used.

2.2. Preparation of OA-OL@CeO_2 superlattice

As described in the introduction section, to obtain NP aggregates, it is necessary to have NPs with spherical morphology and low polydispersion on the radius. For this purpose, we chose cerium oxide nanoparticles (CeO_2-NPs) synthesized at 250 °C in the presence of oleylamine (OL@CeO_2), as the capping agent, based on the experimental results obtained in our previous study[47], which indicated the optimal condition that can guarantee these pre-conditions. Then, OL@CeO_2-NPs were functionalized with oleic acid (OA) to obtain OA-OL@CeO_2 ordered superlattices dispersed in water. Before functionalization, a solvent change was performed. The OL@CeO_2-NPs were centrifuged and recovered in ethyl ether. A specific amount of OA (0.7 mM, in ethyl ether) was dissolved in different amounts (to obtain 14, 20, 30, 50 and 80 mM NPs concentration) of OL@CeO_2-NPs dispersed in ethyl ether. 10 mL of bi-distilled water were added to every organic solution to obtain biphasic systems. These systems were sonicated with a probe tip-sonicator for 5 min to get monophasic systems, which were left under stirring overnight, to remove the organic solvent.

To rationalize the effect of the ordered organization of NPs with respect to a disordered organization on the optical properties of CeO_2-NPs, NaOA-OL@CeO_2 suspensions were prepared as reported in our previous work.[47] The role of NaOA as in the case of OA is to create a further layer around the cluster of oleylamine-coated cerium oxide nanoparticles.

2.3. Dynamic light scattering (DLS)

Dynamic Light Scattering (DLS) analysis was employed to determine the size of functionalized cerium oxide nanoparticles, and to evaluate the time stability in water. DLS measurements were performed using a home-made instrument, composed of a Photocor compact goniometer, an SMD 6000 Laser Quantum 50 mW light source (Quantum Laser, Heaton Mersey, UK) operating at 532.5 nm, a photomultiplier (PMT-120-OP/B), and a correlator (Flex02-01D) from Correlator.com.[47–49] The experiments were carried out at a constant temperature (25.0 ± 0.1) °C, using a thermostatic bath, and at a scattering angle θ of 90°. The hydrodynamic radius was determined from the diffusion coefficient of scattered particles in water. In the approximation of spherical objects, continuous medium, and infinite dilution, the diffusion coefficient can be easily related to the hydrodynamic radius R_h through the Stokes-Einstein equation:

$$R_h = \frac{k_B T}{6\pi\eta D} \quad (1)$$

where k_B is the Boltzmann constant, T is the absolute temperature, and η is the solvent viscosity. For non-spherical particles, R_h corresponds to the radius of spherical particles with the same diffusion coefficient D measured.[50]

2.4. Small Angle X-ray Scattering (SAXS)

Small Angle X-ray Scattering (SAXS) measurements were carried out to determine the ordered structures in which the coated CeO_2-NPs were arranged. SAXS analysis was performed at the beamline B21 of the Diamond Light Source (Didcot, UK). The experiments were carried out at 25 °C. The beamline configuration was with a beam energy of 12.4 keV, and a sample-to-detector distance of 3.7 m. This configuration allowed us to collect the data for the scattering vector modulus $Q = 4\pi sin(\theta/2)/\lambda$ in the range of values between 0.0026 $Å^{-1}$ and 0.34 $Å^{-1}$, where θ is the scattering angle.[51]

2.5. Transmission Electron Microscopy (TEM)

Transmission Electron Microscopy (TEM) images were acquired to investigate the morphology of CeO_2-NPs and OA-OL@CeO_2 NPs, using as microscope the FEI TECNAI G2 200 kV (Fei Company, Dawson Creek Drive Hillsboro, Hillsboro, OR USA). Approximately 10 μL of a given sample was placed on a carbon-coated copper grid and allowed to air dry before imaging.[47]

2.6. Cryogenic Transmission Electron Microscopy (Cryo-TEM)

Cryogenic Transmission Electron Microscopy (Cryo-TEM) measurements were performed to characterize superlattice structures and to determine the parameters that drive the hierarchical organization. Cryo-TEM images were carried out at Heinz Maier-Leibnitz Source, Garching Forschungzentrum (Germany), on a JEOL 200 kV JEM-FS2200 with a field emission gun (FEG). Samples for Cryo-TEM were prepared by placing a 5 μL drop of superlattice suspension on a Quantifoil Multi A carbon-coated copper grid. After, the sample was cryo-fixed by rapidly immersing it into liquid ethane at −180 °C in a cryo-plunge (EMGP Leica GmbH). The grid was inserted into a cryo-transfer holder (HTTC 910, Gatan, Munich, Germany), and transferred to a JEM 2200 FS EFTEM instrument (JEOL, Tokyo, Japan). Examinations were carried out at a temperature of around −180 °C. The transmission electron microscope was operated at an acceleration voltage of 200 kV. All images were recorded digitally by a bottom-mounted 16-bit CMOS camera system (TemCam-F2016, TVIPS, Munich, Germany). Images were taken with the EMenu 4.0 image acquisition program (TVIPS, Munich, Germany) and processed with a free digital imaging processing system, ImageJ.

2.7. Fluorescence spectroscopy

Fluorescence spectra were carried out to investigate the optical properties of OA-OL@CeO_2 and NaOA-OL@CeO_2 aggregates in suspension. Horiba Scientific Fluoromax-4 spectrofluorometer (Horiba France SAS, JobinYvon, Palaiseau, France) equipped with a Peltier control system and 1 cm path length cells was used. To eliminate the scattering of samples, measurements were conducted using polarizers. Each sample was excited at 305 nm, with an integration time of 0.1 s, and excitation, and an emission slit width of 5 nm.[47]

2.8. Photoluminescence excitation spectroscopy (PLE)

An in-house setup for excitation-resolved photoluminescence (PLE) was used to analyze the optical properties of OA-OL@CeO_2 superlattice suspensions. The PLE setup provided wavelength-tunable incoherent light to excite and collect the photoluminescence (PL) of a sample placed in a controlled environment and the use of a double-lens confocal optical system to collect the PL spectral intensity, described in further detail in previous work. [52,53] Excitation light at variable central wavelength spanning in the interval from 340 nm to 420 nm (FWHM of the excitation line approximately 2 nm) was provided by a monochromatized Xe lamp, collected by a liquid waveguide and focused on the samples, which consisted of 200 μL droplets of OA-OL@CeO_2 or NaOA-OL@CeO_2 aqueous suspensions dropped onto an aluminum substrate placed into the optical chamber. The PL light was collected by a multi-mode 1000 μm core optical fiber and sent to a motorized monochromator of 320 mm equivalent focal length, equipped with a cooled CCD camera for spectral acquisition. Before detection, the light emerging from the samples was filtered off the spectral components of wavelengths shorter than 420 nm to avoid the detection of spurious signals originating from the excitation light and to reduce a residual Raman signal originating from the liquid

waveguide. The residual signal measured from the Al substrate and the pure solvent (i.e., water droplets) was largely negligible with respect to the ones detected for the dispersions of functionalized CeO_2 NPs.

3. Result and discussion

3.1. Cerium oxide nanoparticles coated with oleylamine (OL@CeO_2-NPs)

CeO_2-NPs were synthesized through the thermal decomposition of cerium(III) nitrate hexahydrate at 250 °C using oleylamine (OL) as a capping agent. After dispersion in chloroform, such coated NPs (OL@CeO_2 NPs) revealed a monodispersed system showing a spherical shape and a hydrodynamic radius of 5 nm, which corresponds to the sum between the inorganic core, with an average radius of about 2.5 nm, and the length of the alkyl chain of the OL, calculated using the Tanford equation, of about 2.5 nm, as represented in Fig. 1.[47]

3.2. OL@CeO_2-NPs functionalized with oleic acid (OA-OL@CeO_2 NPs)

Clusters of ordered nanoparticles were obtained through the emulsion method by using different amounts of OL@CeO_2-NPs and a constant concentration of oleic acid (OA), see Table 1. OL@CeO2-NPs are coated with OA molecules that create a second organic layer around the NPs whose surface is hydrophilic and allows their dispersion in a polar medium such as water.

The formation of the aggregates in suspension was assessed through DLS measurements. Hydrodynamic radius R_h values between 160 and 350 nm (Table 2) were obtained on the first day after functionalization and remained constant for about 3 weeks (Figure S1). This result indicates that the aggregates of NPs formed during the functionalization process and not *via* a successive coalescence of neighboring nanoparticles. The measured size of the clusters agrees with those obtained by a micro-emulsion method, as reported by Wei *et al.*.[33] Among the forces that drive the formation of aggregates, elastic and hydrophobic ones play a key role in driving the self-assembly process for the systems.

The superlattice structures were investigated by combining SAXS, TEM, and Cryo-TEM analyses. The choice of using a multi-methodologic approach lies in investigating the structural and morphological properties of these aggregates both in solution and dry, to demonstrate that the obtained superlattices are stable in water as well as in their absence.

Cryomicroscopy images collected on three samples (OA-OL@CeO2_50,_20, and_14) revealed the simultaneous presence of different structural motifs (Fig. 2 and S2), the relative contribution of which is related to the amount of OL@CeO_2.

The ability of the decorated CeO_2-NPs to adopt different structural organizations was confirmed by SAXS measurements. In particular, the diffraction profile of OA-OL@CeO_2_50 and OA-OL@CeO_2_20 samples differ from that of the others (Table 2, Figs. 3, 5, and S7).

Table 1
Summary of different samples of superlattice CeO_2-NPs.

Sample	OL@CeO_2-NPs [mM]	OA [mM]
OA-OL@CeO_2_80	80	0.7
OA-OL@CeO_2_50	50	0.7
OA-OL@CeO_2_30	30	0.7
OA-OL@CeO_2_20	20	0.7
OA-OL@CeO_2_14	14	0.7

3.3. C14 Frank-Kasper phase: OA-OL@CeO_2_50 and OA-OLCeO_2_20

The analysis of SAXS patterns for OA-OL@CeO_2_50 and OA-OL@CeO_2_20 samples revealed structure factor peaks typical of a hexagonal phase. The experimental values of Q/Q_1 (Table S1) are comparable to that of a Frank-Kasper phase with a hexagonal unite cell (C14 phase), the values resulting very close (Table S1). The presence of the hexagonal phase was also confirmed by electron microscopy images which were collected both at room (Fig. 3C-E) and cryogenic temperature (Fig. 4 A-F). TEM images collected on dry samples reveal that the ordered structure is preserved upon solvent evaporation.

In particular, the analysis of Cryo-TEM images showed traces of a distorted compact hexagonal-type structure with lattice parameters $a = b \sim 9.0$ nm, $c \sim 14.7$ nm, and $\gamma \sim 115°$.

NP arrangement in a honeycomb structure, typical of Frank-Kasper phases (each nanoparticle in these structures is surrounded by 12 neighbors), was also identified in the same images, as shown in Fig. 4D, E, and F.

3.4. Face-centered cubic (FCC) phase: OA-OL@CeO_2_14

The SAXS pattern for the OA-OL@CeO_2_14 sample (Fig. 5A) revealed structure factor peaks consistent with an FCC symmetry and a unit cell dimension $a \sim 14.3$ nm. Indeed, in a SAXS profile the scattering peaks with position ratio of 1:(4/3)1/2:(8/3)1/2:(11/3)1/2…. and Miller indices (1 1 1), (2 0 0), (2 2 0), (3 1 1)…. are signatures for the FCC lattice. The Q/Q_1 ratio, the characteristic peaks, as well as the interplanar distance d_{hkl}, and the size of the elementary cell $\boldsymbol{a}$, are shown in Table S3. The presence of an FCC phase is detectable in the TEM images of this sample and the corresponding Fourier transform (Fig. 5B, C, and D). Also, the Cryo-TEM image revealed features in line with the SAXS data (Fig. 5E, F, and G). The region highlighted in Fig. 5F showed orthogonal

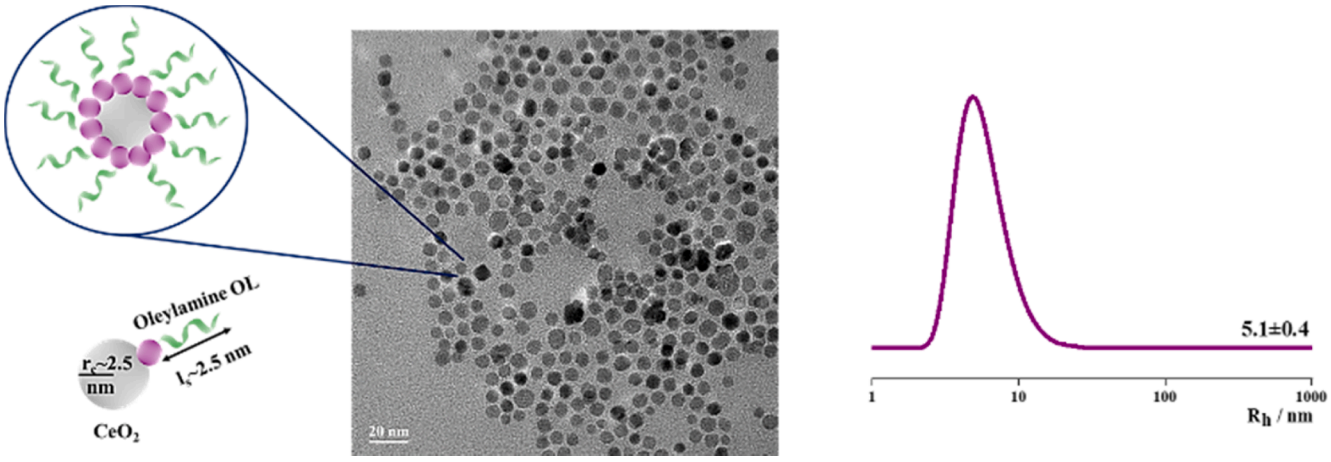

Fig. 1. Schematic representation of OL@CeO_2 NPs, TEM image of OL@CeO_2 NPs (scale bar: 20 nm), and hydrodynamic radius distribution of OL@CeO_2 NPs in chloroform.

Table 2
Inorganic core radius, organic layers on NP surface, hydrodynamic radius of the aggregate, and prevalent ordered structures observed for OA-OL@CeO_2_80, OA-OL@CeO_2_50, OA-OL@CeO_2_30, OA-OL@CeO_2_20, and OA-OL@CeO_2_14 samples.

Sample	Inorganic core radius/nm	Organic Layers	Aggregate hydrodynamic radius/nm	Prevalent ordered structure
OA-OL@CeO_2_80	2.5	oleylamine + oleic acid	430 ± 70	Face-centered cubic (FCC)
OA-OL@CeO_2_50	2.5	oleylamine + oleic acid	166 ± 4	Frank-Kasper (FK-C14)
OA-OL@CeO_2_30	2.5	oleylamine + oleic acid	360 ± 20	Face-centered cubic (FCC)
OA-OL@CeO_2_20	2.5	oleylamine + oleic acid	290 ± 20	Frank-Kasper (FK-C14)
OA-OL@CeO_2_14	2.5	oleylamine + oleic acid	350 ± 20	Face-centered cubic (FCC)

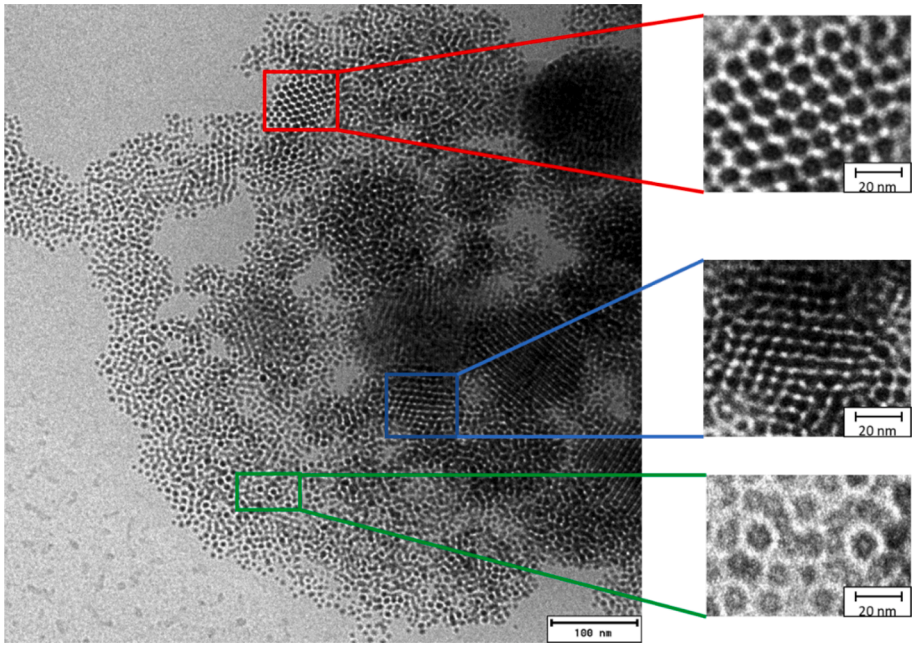

Fig. 2. Cryo-TEM image. The marked regions (enlarged sections, scale bar: 20 nm) show different local organizations of OA-OL@CeO_2_20 in D_2O (scale bar: 100 nm).

rows with a d_m spacing of ~ 7.15 nm, consistent with the projection along the ***c*** axis of an FCC lattice having an axis ***a*** ~ 14.3 nm.

The small difference in the free energy of Frank-Kasper and FCC structural organizations, with entropy marginally favoring the FCC structure,[54] may result in phase coexistence. TEM and Cryo-TEM images suggested that the face-centered cubic and the distorted hexagonal close-packed crystal structures coexisted in OA-OL@CeO_2 NPs samples. However, the hexagonal phase prevailed in the OA-OL@CeO_2_50 and OA-OL@CeO_2_20 ones, while the FCC phase was dominant in OA-OL@CeO_2_80, OA-OL@CeO_2_30, and OA-OL@CeO_2_14 samples, as noted by SAXS. These findings can be explained by considering that, differently from the hard spheres, the conformational flexibility provided by the soft shell of the decorated NPs can favor a greater adaptation to the local constraints thus inducing the coexistence of two phases with comparable thermodynamic stability.[55]

3.5. OA-OL@CeO_2 NPs: Optical properties

The emission properties of OA-OL@CeO_2 systems were initially analyzed by fluorescence spectroscopy using the previously described fluorescence (Fluoromax) system. In Fig. 6 we show the spectra obtained for the various ordered systems at different NP concentrations (80, 50, 30, 20, and 14 mM; Fig. 6A) and compare them with the corresponding disordered ones (Fig. 6B) as obtained by functionalizing the OL@CeO_2 NPs with NaOA.

The emission of the ordered systems (Fig. 6A) is visibly higher than that of the disordered systems (Fig. 6B). Moreover, in the case of NaOA-OL@CeO_2 samples, the fluorescence intensity increases with the concentration of NPs forming the system (Fig. 6B). In contrast, for the samples with a hierarchical organization, a fluorescence intensity trend independent of NPs concentration is observed, which could probably depend on the relative amount of the different phases included in the system (Fig. 6A).

Fig. 7 shows PLE maps of the investigated samples OA-OL@CeO_2_50, NaOA-OL@CeO_2_50, OA-OL@CeO_2_20, and NaOA-OL@CeO_2_20 (Panels A, B, D and E, respectively), along with a comparison of the PL spectra using comparable intensity units obtained at the same excitation wavelength (λ_{exc} = 380 nm). Here, by "PLE map" it means the superposition of PL intensity spectra obtained at different values of excitation spectra, i.e., the quantity I(λ_{PL}, λ_{exc}), where I is the measured PL signal expressed in counts-*per*-second (cps) units, λ_{PL} is the photoluminescence (i.e., emission) wavelength and λ_{exc} is the excitation wavelength. No significant tests could be performed for the samples at lower CeO_2 concentrations (i.e., 14 mM) due to the almost negligible intensity of the PL signal which led to an unfavorable signal-to-noise ratio. It is to be noted that the short wavelength spectral tails of photoluminescence (i.e., wavelength shorter than 420 nm) are absent from the maps and graphs of Fig. 7, due to the need to use a longwave-pass sharp cut-off filter to block the excitation stray light and residual Raman emission generated by the liquid waveguide (as discussed in experimental section). We underline that the PLE data reported in Fig. 7 are collected via an experimental setup different from the one used for the spectra in Fig. 6, justifying the differences in the spectral shape of the respective PL intensities.

The top row of Fig. 7 reports data all referring to the samples of suspension whose concentration of CeO_2 was 50 mM, while the bottom row refers to 20 mM suspensions. The first two maps (Panels A and B) allow for a comparison of the PLE intensity maps obtained for the Frank-

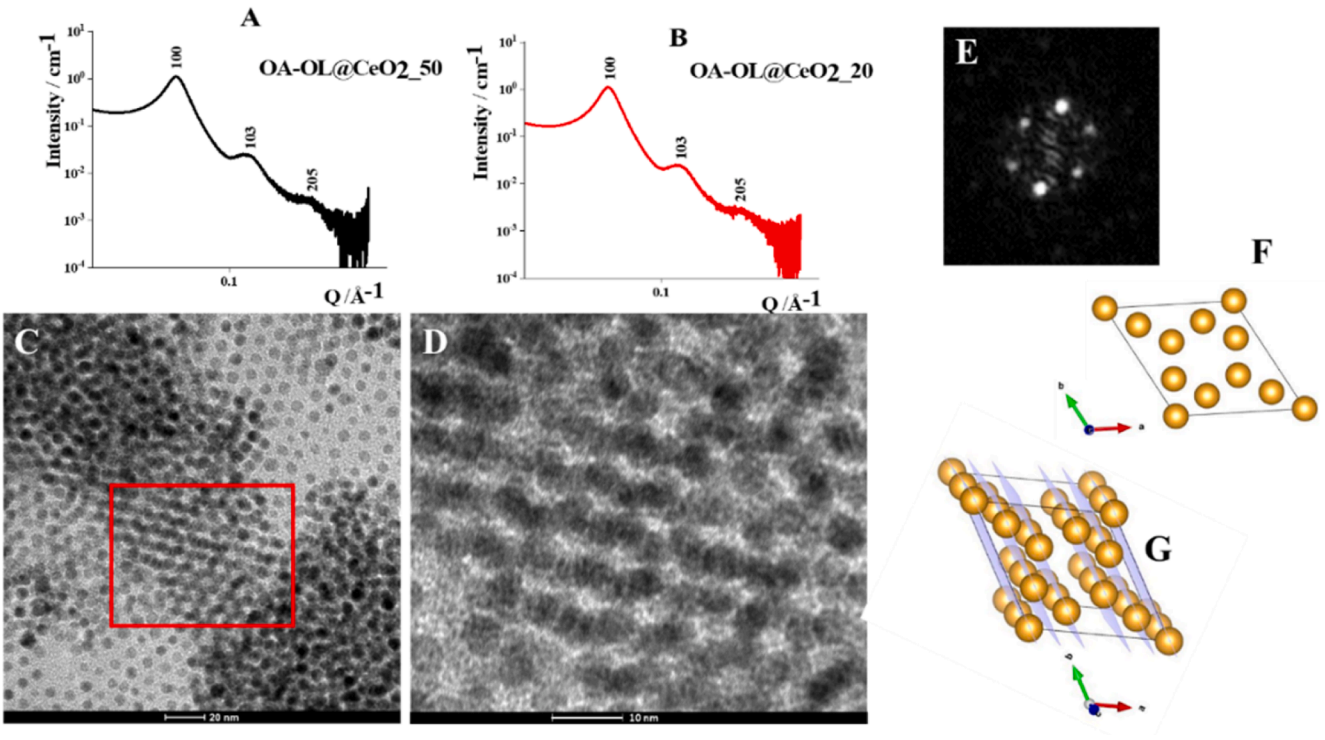

Fig. 3. SAXS pattern of OA-OL@CeO_2_50 in H_2O **(A)**; SAXS pattern of OA-OL@CeO_2_20 in H_2O **(B)**; TEM image of OA-OL@CeO_2_20 with a hexagonal structure, scalebar: 20 nm **(C)**; enlarged section of the region marked in C, scalebar: 10 nm **(D)**; FTT calculated on the area marked in C **(E)**; 2D schematic representation of C14 phase **(F)**; 3D schematic representation of C14 phase **(G)**.

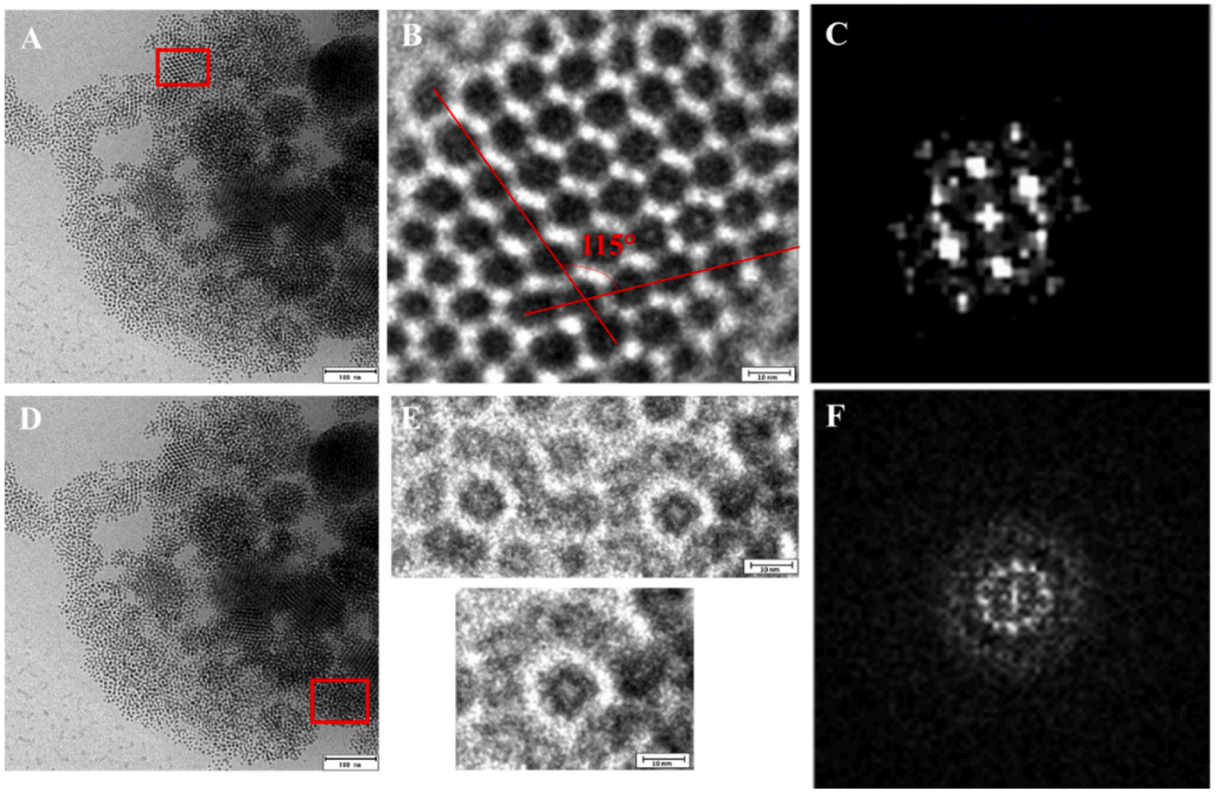

Fig. 4. Cryo-TEM image of OA-OL@CeO_2_20 with a hexagonal structure in D_2O, scalebar: 100 nm **(A)**; enlarged section of the region marked in A, scalebar: 10 nm **(B)**; FTT of the region shown in B **(C)**; Cryo-TEM image of OA-OL@CeO_2_20 with a honeycomb structure in D_2O, scalebar: 100 nm **(D)**; enlarged section of the region marked in D, scalebar: 10 nm **(E)**; FTT of the region shown in E **(F)**.

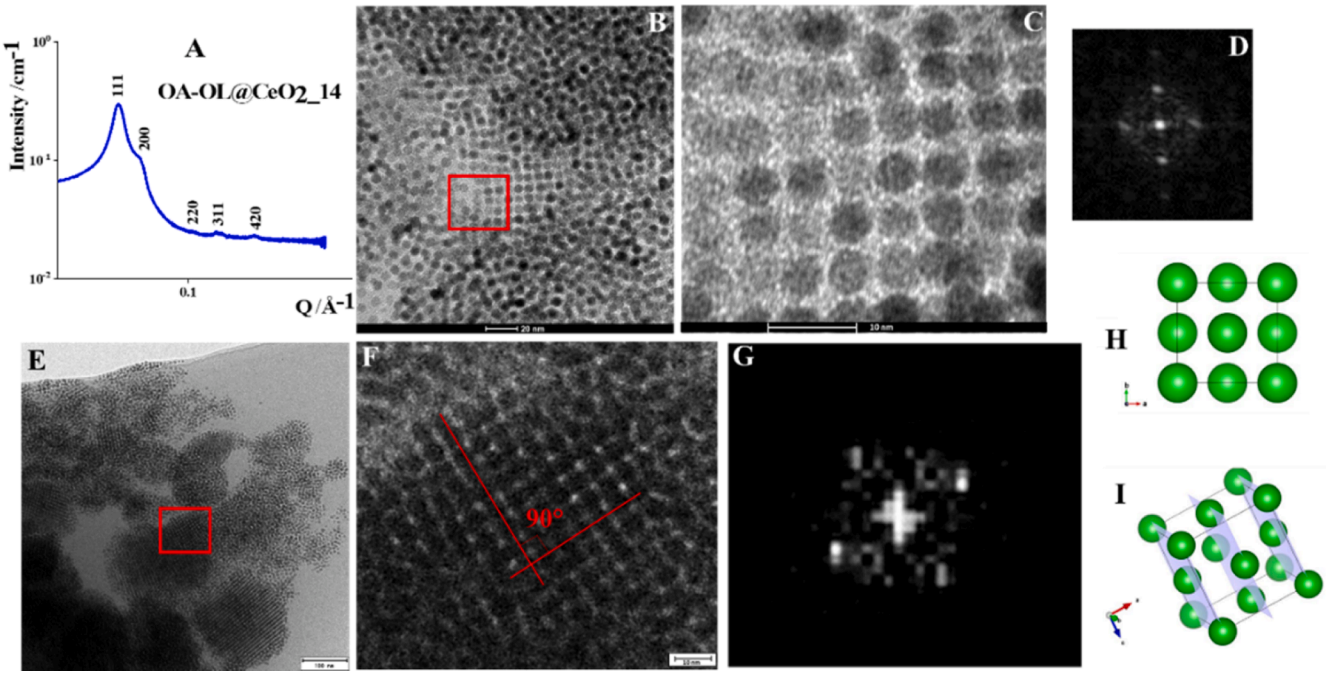

Fig. 5. SAXS pattern of OA-OL@CeO_2_14 in H_2O **(A)**; TEM image of OA-OL@CeO_2_14 with a FCC structure, scalebar: 20 nm **(B)**; enlarged section of B image, scalebar: 10 nm **(C)**; FTT of the region shown in C **(D)**; Cryo-TEM image of OA-OL@CeO_2_14 in D_2O, scalebar: 100 nm **(E)**; enlarged section of the region marked in E, scalebar: 10 nm **(F)**; FTT of the region shown in F **(G)**; 2D schematic representation of FCC phase **(H)**; 3D schematic representation of FCC phase **(I)**.

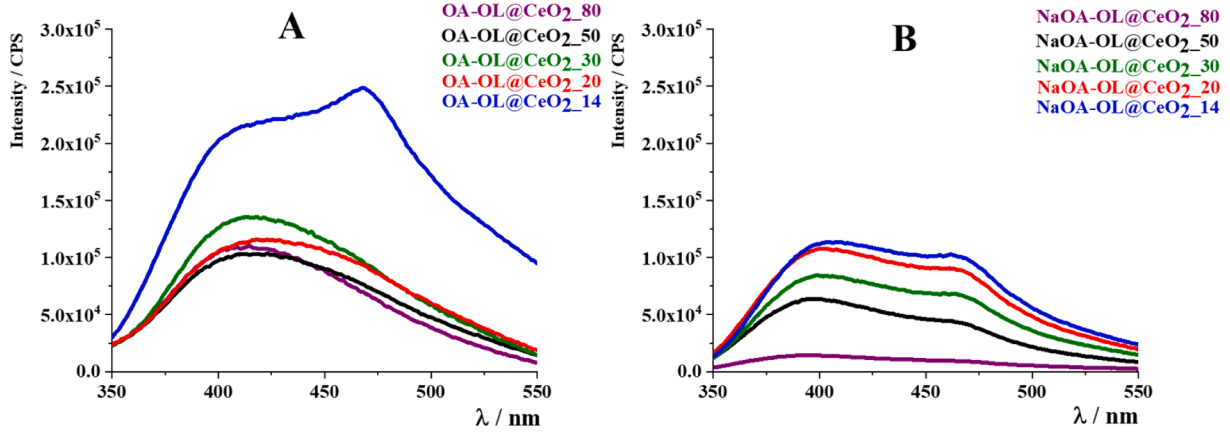

Fig. 6. Fluorescence spectra of OA-OL@CeO_2_80 (purple line), OA-OL@CeO_2_50 (black line), and OA-OL@CeO_2_30 (green line), OA-OL@CeO_2_20 (red line), and OA-OL@CeO_2_14 (blue line) in water **(A)**; fluorescence spectra of NaOA-OL@CeO_2_80 (purple line), NaOA-OL@CeO_2_50 (black line), and NaOA-OL@CeO_2_30 (green line), NaOA-OL@CeO_2_20 (red line), and NaOA-OL@CeO_2_14 (blue line) in water **(B)**. (For interpretation of the references to colour in this figure legend, the reader is referred to the web version of this article.)

Kasper structured superlattice (Fig. 7A) *vs.* the one relative to a disordered dispersed homogeneous suspension (Fig. 7B). It is easily noticeable that, while the qualitative features of the excitation-emission phenomena appear to be the same based on the similarity of the maps, the absolute intensity of the signal differs significantly: a much larger PL emission is detected for the ordered superlattices, as evidenced by the difference in the intensity range used to plot Fig. 7A and 7B. This point can be more easily visualized via the direct comparison of the PL intensity spectra reported in Fig. 7C, where the black and the red curves refer to the Frank-Kasper superlattice and disordered dispersion, respectively (please note that the intensity units are comparable) acquired under excitation at $\lambda_{exc} = 380$ nm. The same conclusions can be deduced from the experiments performed on samples of the 20 mM solutions. It is to be underlined that we experimentally verified that the differences in PL intensities exhibited by the two kinds of suspensions are statistically significant. The data reported in Fig. 7 are the averages over repeated measurements on multiple samples for each suspension. Six PLE maps were performed for each of the four suspensions reported, finding a relative uncertainty of about 15 % (standard deviation divided by mean) for sample-to-sample repeated measurements of intensity, which is significantly lesser than the intensity variation (300 % – 400 %, see Fig. 7C and 7F) determined for Frank-Kasper *vs.* ordinary suspensions.

The data indicate a specific link between the enhancement of PL intensity and the aggregation of the CeO_2 nanoparticles in ordered aggregates. Some hypotheses about the nature of such correlation can be formulated and are discussed below.

The occurrence of amplification of luminescence intensity caused by the aggregation of individual luminophores has been observed in some classes of organic molecules and schematized in the so-called

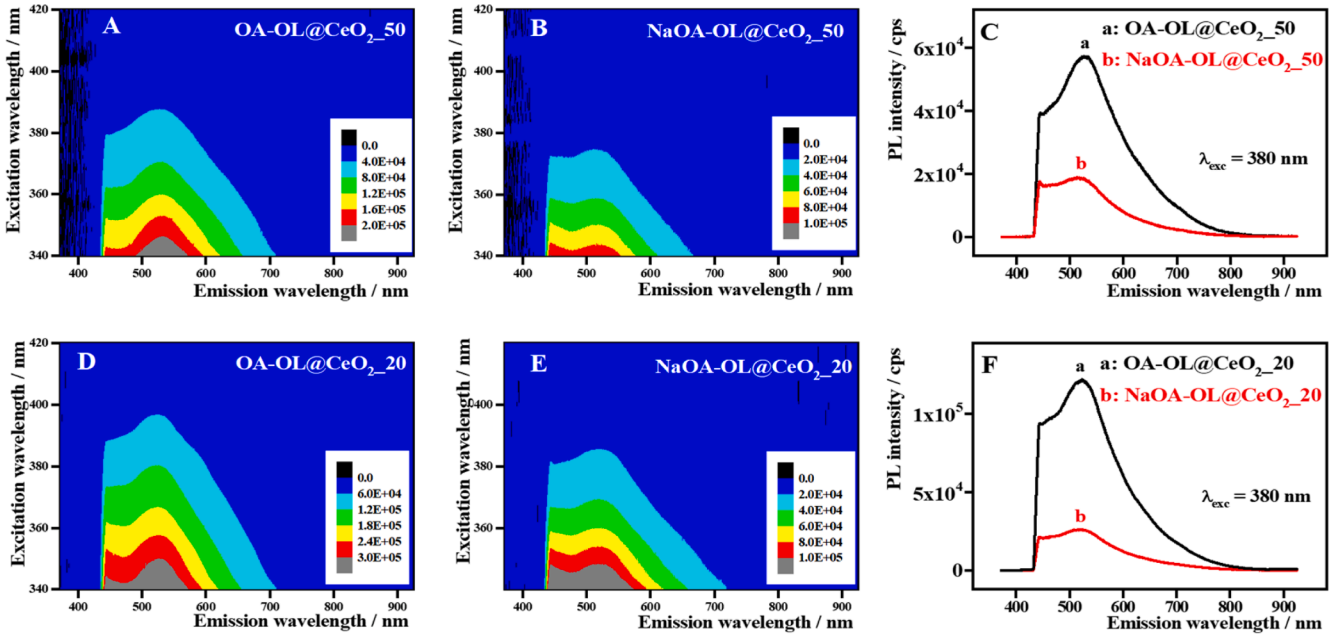

Fig. 7. The upper row (7A, 7B, and 7C) refers to the experimental data obtained for the structured (OA-OL@CeO_2_50) and randomly dispersed non-structured (NaOA-OL@CeO_2_50) suspensions with 50 mM NPs concentration. **(A)**: PLE intensity maps of OA-OL@CeO_2_50, **(B)**: PLE intensity map of NaOA-OL@CeO_2_50, **(C)** PL spectra of the two samples obtained for 380 nm excitation. The lower row (7D, 7E and 7F) represents the same quantities obtained for the suspensions of 20 mM concentrations, i.e. **(D)**: PLE intensity maps of OA-OL@CeO_2_20, €: PLE intensity map of NaOA-OL@CeO_2_20, **(F)** PL spectra of the two samples obtained for 380 nm excitation. All the data reported are obtained by averaging the experimental results over a set of six repeated measurements.

phenomenon of AIEE (namely: "aggregation-induced emission enhancement"), firstly reported in the case of helix-shaped organic molecules.[56] AIEE has been described as the consequence of the suppression of non-radiative decays of excited states of the molecules, caused by aggregation-induced inhibition of molecular rotation.[57,58] Obviously, this mechanism cannot be invoked in cases such as ours where the luminophores are semiconductor nanoparticles, whose PL emission intensity is typically regulated by the density of non-radiative traps. However, the experimental evidence and the analogy with AIEE suggest that some aggregation-related mechanism that quenches the non-radiative recombination and/or enhances the radiative recombination charge carriers in CeO_2 shall be at work.

Interestingly, a similar phenomenon was described by Jassby and Wiesner in their work about the aggregation-induced PL enhancement in ZnS nanoparticles.[59] The authors found out that aggregation favored the band-edge PL of ZnS nanoparticles, a phenomenon that they proposed to be caused by the reduction of surface tension of the semiconductor nanocrystals determined by the increase in the van der Waals forces caused by particle aggregation. They argued that the decrease of surface tension in the crystal has been often associated with an increase in PL emission due to the reduction of strain caused by point defects and the consequent decrease in the number of electron traps acting as non-radiative centers.[60,61] The role of electron traps is played by sulfur vacancies in ZnS, and more in general, by oxygen vacancies in a metal oxide. Specifically, lattice strain favors the formation of O vacancies on CeO_2, so that the mechanism observed for ZnS can be suggested to be at work also in our case. Moreover, as also pointed out by Jassby and co-workers,[59] NP aggregation can also determine the passivation of surface traps and dangling bonds caused by the presence of neighboring particles in the close-packed Frank-Kasper aggregate, again determining a decrease in the probability of non-radiative electron-hole recombination.

As another possible interpretation for the phenomenon, we suggest that it might be caused by an improvement in the excitation efficiency caused by Foster resonant energy transfer. The emission of the isolated CeO_2 particle is of course proportional to its absorption cross-section. Hence, isolated NPs floating in suspension will be able to convert the excitation energy into PL emission only proportionally to the photons absorbed by them. However, once the NPs are closely packed forming the Frank-Kasper superlattice, with an interparticle distance of the order 1–2 nm intercalated by the amphiphilic molecules, the absorption cross-section of this latter can also contribute indirectly to PL via Förster energy transfer. For example, this type of indirect PL excitation is well known in cases where the emission of small luminophores, e.g. lanthanide ions, is amplified by the "antenna effect" operated by nearby donor species.[62,63] In our case, we may suggest the amphiphiles act as donor species. It is worth remembering that Förster energy transfer occurs at an efficiency proportional to the inverse sixth power of the distance between donor and acceptors so that only at very close distances (i.e., dense packings, as observed in Figs. 3-5) the amplification effect shall be relevant.

4. Conclusions

In this work, we experimentally observed the organization of coated cerium oxide nanoparticles in a regular superlattice. CeO_2 nanoparticles of a 5 nm radius with low polydispersity and spherical shape coated with long amphiphilic molecules, such as oleylamine, through a two-step procedure, were assembled in a regular spatial arrangement. The 3D organization was obtained at the nanoscale level and extends down to 200–300 nm. In all cases, the coexistence of face-centered cubic and Frank-Kasper phases with a hexagonal unit cell was observed, although at high concentrations the system is dominated by the second phase. Indeed, at 14 mM NP concentration a face-centered cubic structure prevails. On the opposite, the 20 and 50 mM NP concentrations stabilize the Frank-Kasper phase. Photoluminescence measurements clearly show that the intrinsic fluorescence of cerium oxide nanoparticles is amplified by a factor of 3–4 (i.e., 300 %-400 %) when the spatial organization of the particles is ordered. These results can be interpreted based on a decrease in the probability of non-radiative recombination between

electrons and holes or an improvement in excitation efficiency due to Förster 's resonant energy transfer.

The results obtained highlight the key role of amphiphilic-mediated strategy in driving the formation of 3D superstructures with advanced optical properties. In particular, the chemical nature of the amphiphiles used to coat inorganic nanoparticles is decisive in regulating the generation of ordered or disordered structures in aqueous solution. Differences in chain length or the nature of polar head groups, as well as different concentration, could be useful in identifying the driving forces leading to different ordered superstructures with adjustable optical properties for technological applications. For example, quantum dots (QDs) are interesting fluorescent materials for biological imaging due to their spectral tuning in the visible and infrared regions. Individual QDs, while possessing high quantum yields, are sometimes insufficiently bright due to their small size. However, colloidal cluster structures assembled from primary QDs can provide much stronger signals in biological imaging[64]. In addition, colloidal cluster structures may exhibit collective properties not present in individual nanoparticles. A classic example is the clustering of noble metal nanoparticles for generating "hot spots" to enhance Raman scattering. The assembly of plasmonic nanoparticles into secondary structures can induce near-field electromagnetic coupling of surface plasmons between adjacent particles, thus creating "hot spots" that can significantly enhance Raman signals from analytes.[65,66]

The ability to modulate the organization of nanoparticles opens the possibility of developing systems to be applied in different technological fields with superior properties. In this particular case, the original optical properties of cerium oxide are greatly amplified if they are arranged in an ordered system. Similarly, one is likely to have the same result with particles with different properties such as magnetic, and catalytic for many further technological applications.

CRediT authorship contribution statement

Noemi Gallucci: Data curation, Investigation, Writing – original draft. **Marie-Sousai Appavou:** Investigation. **Nathan Cowieson:** Investigation. **Gerardino D'Errico:** Writing – review & editing. **Rocco Di Girolamo:** Data curation, Investigation, Validation. **Stefano Lettieri:** Data curation, Formal analysis, Investigation, Writing – original draft, Writing – review & editing. **Filomena Sica:** Data curation, Investigation, Validation. **Giuseppe Vitiello:** Data curation, Investigation, Writing – original draft, Writing – review & editing. **Luigi Paduano:** Conceptualization, Data curation, Funding acquisition, Project administration, Resources, Supervision, Writing – original draft, Writing – review & editing.

Declaration of competing interest

The authors declare that they have no known competing financial interests or personal relationships that could have appeared to influence the work reported in this paper.

Data availability

Data will be made available on request.

Acknowledgments

This project has received funding from the European Union's Horizon 2020 research and innovation program under grant agreement No 101007417 having benefitted from the access provided by the Jülich Centre for Neutron Science at the Meier Leibnitz Zentrum in Garching bei München, Germany within the framework of the NFFA-Europe Pilot Transnational Access Activity (nffa.eu), proposal ID677.

Appendix A. Supplementary data

Supplementary data to this article can be found online at https://doi.org/10.1016/j.jcis.2024.01.029.

References

[1] Z. Lu, Y. Yin, Colloidal Nanoparticle Clusters: Functional Materials by Design, Chem. Soc. Rev. 41 (21) (2012) 6874–6887, https://doi.org/10.1039/C2CS35197H.
[2] J.K. Stolarczyk, A. Deak, D.F. Brougham, Nanoparticle Clusters: Assembly and Control Over Internal Order, Current Capabilities, and Future Potential, Adv. Mater. 28 (27) (2016) 5400–5424, https://doi.org/10.1002/adma.201505350.
[3] N.S. Mueller, E. Pfitzner, Y. Okamura, G. Gordeev, P. Kusch, H. Lange, J. Heberle, F. Schulz, S. Reich, Surface-Enhanced Raman Scattering and Surface-Enhanced Infrared Absorption by Plasmon Polaritons in Three-Dimensional Nanoparticle Supercrystals, ACS Nano 15 (3) (2021) 5523–5533, https://doi.org/10.1021/acsnano.1c00352.
[4] J.N. Israelachvili, Intermolecular and Surface Forces, Academic Press, 2011.
[5] H.B.G. Casimir, D. Polder, The Influence of Retardation on the London-van Der Waals Forces, Phys. Rev. 73 (4) (1948) 360–372, https://doi.org/10.1103/PhysRev.73.360.
[6] H.C. Hamaker, The London—van Der Waals Attraction between Spherical Particles, Physica 4 (10) (1937) 1058–1072, https://doi.org/10.1016/S0031-8914(37)80203-7.
[7] S. Bhattacharjee, M. Elimelech, Surface Element Integration: A Novel Technique for Evaluation of DLVO Interaction between a Particle and a Flat Plate, J. Colloid Interface Sci. 193 (2) (1997) 273–285, https://doi.org/10.1006/jcis.1997.5076.
[8] I.E. Dzyaloshinskii, E.M. Lifshitz, L.P. Pitaevskii, The General Theory of van Der Waals Forces, Adv. Phys. 10 (38) (1961) 165–209, https://doi.org/10.1080/00018736100101281.
[9] J. Stenhammar, P. Linse, H. Wennerström, G. Karlström, An Exact Calculation of the van Der Waals Interaction between Two Spheres of Classical Dipolar Fluid, J. Phys. Chem. B 114 (42) (2010) 13372–13380, https://doi.org/10.1021/jp105754t.
[10] K.J.M. Bishop, C.E. Wilmer, S. Soh, B.A. Grzybowski, Nanoscale Forces and Their Uses in Self-Assembly, Small 5 (14) (2009) 1600–1630, https://doi.org/10.1002/smll.200900358.
[11] J. Belloni, M. Mostafavi, H. Remita, J.-L. Marignier, M.-O. Delcourt, Radiation-Induced Synthesis of Mono- and Multi-Metallic Clusters and Nanocolloids, New J. Chem. 22 (11) (1998) 1239–1255, https://doi.org/10.1039/A801445K.
[12] A.M. Kalsin, M. Fialkowski, M. Paszewski, S.K. Smoukov, K.J.M. Bishop, B. A. Grzybowski, Electrostatic Self-Assembly of Binary Nanoparticle Crystals with a Diamond-Like Lattice, Science 312 (5772) (2006) 420–424, https://doi.org/10.1126/science.1125124.
[13] A.M. Kalsin, A.O. Pinchuk, S.K. Smoukov, M. Paszewski, G.C. Schatz, B. A. Grzybowski, Electrostatic Aggregation and Formation of Core−Shell Suprastructures in Binary Mixtures of Charged Metal Nanoparticles, Nano Lett. 6 (9) (2006) 1896–1903, https://doi.org/10.1021/nl060967m.
[14] T.C. Preston, M. Nuruzzaman, N.D. Jones, S. Mittler, Role of Hydrogen Bonding in the pH-Dependent Aggregation of Colloidal Gold Particles Bearing Solution-Facing Carboxylic Acid Groups, J. Phys. Chem. C 113 (32) (2009) 14236–14244, https://doi.org/10.1021/jp903284h.
[15] D. Wang, B. Kowalczyk, I. Lagzi, B.A. Grzybowski, Bistability and Hysteresis During Aggregation of Charged Nanoparticles, J. Phys. Chem. Lett. 1 (9) (2010) 1459–1462, https://doi.org/10.1021/jz100406w.
[16] *Nanoparticle Aggregation Controlled by Desalting Kinetics | The Journal of Physical Chemistry C*. https://pubs.acs.org/doi/full/10.1021/jp904665u (accessed 2023-11-06).
[17] M. Meyer, E.C. Le Ru, P.G. Etchegoin, Self-Limiting Aggregation Leads to Long-Lived Metastable Clusters in Colloidal Solutions, J. Phys. Chem. B 110 (12) (2006) 6040–6047, https://doi.org/10.1021/jp055866b.
[18] J. Zhuang, H. Wu, Y. Yang, Y.C. Cao, Supercrystalline Colloidal Particles from Artificial Atoms, J. Am. Chem. Soc. 129 (46) (2007) 14166–14167, https://doi.org/10.1021/ja076494i.
[19] J. Zhuang, H. Wu, Y. Yang, Y.C. Cao, Controlling Colloidal Superparticle Growth Through Solvophobic Interactions, Angew. Chem. Int. Ed. 47 (12) (2008) 2208–2212, https://doi.org/10.1002/anie.200705049.
[20] S.H. Donaldson Jr., A. Røyne, K. Kristiansen, M.V. Rapp, S. Das, M.A. Gebbie, D. W. Lee, P. Stock, M. Valtiner, J. Israelachvili, Developing a General Interaction Potential for Hydrophobic and Hydrophilic Interactions, Langmuir 31 (7) (2015) 2051–2064, https://doi.org/10.1021/la502115g.
[21] A. Sánchez-Iglesias, M. Grzelczak, T. Altantzis, B. Goris, J. Pérez-Juste, S. Bals, G. Van Tendeloo, S.H. Donaldson Jr., B.F. Chmelka, J.N. Israelachvili, L.M. Liz-Marzán, Hydrophobic Interactions Modulate Self-Assembly of Nanoparticles, ACS Nano 6 (12) (2012) 11059–11065, https://doi.org/10.1021/nn3047605.
[22] B. Pansu, C. Goldmann, D. Constantin, M. Impéror-Clerc, J.-F. Sadoc, Softness-Driven Complexity in Supercrystals of Gold Nanoparticles, Soft Matter 17 (26) (2021) 6461–6469, https://doi.org/10.1039/D1SM00617G.
[23] B.W. Goodfellow, Y. Yu, C.A. Bosoy, D.-M. Smilgies, B.A. Korgel, The Role of Ligand Packing Frustration in Body-Centered Cubic (Bcc) Superlattices of Colloidal Nanocrystals, J. Phys. Chem. Lett. 6 (13) (2015) 2406–2412, https://doi.org/10.1021/acs.jpclett.5b00946.

[24] Y. Liu, H. Nie, R. Bansil, M. Steinhart, J. Bang, T.P. Lodge, Kinetics of Disorder-to-Fcc Phase Transition via an Intermediate Bcc State, Phys. Rev. E 73 (6) (2006) 061803, https://doi.org/10.1103/PhysRevE.73.061803.

[25] H. Takagi, R. Hashimoto, N. Igarashi, S. Kishimoto, K. Yamamoto, Synchrotron SAXS Studies on Lattice Structure of Spherical Micelles in Binary Mixtures of Block Copolymers and Homopolymers, J. Fiber Sci. Technol. 74 (1) (2018) 10–16, https://doi.org/10.2115/fiberst.2018-0002.

[26] K. Yue, M. Huang, R.L. Marson, J. He, J. Huang, Z. Zhou, J. Wang, C. Liu, X. Yan, K. Wu, Z. Guo, H. Liu, W. Zhang, P. Ni, C. Wesdemiotis, W.-B. Zhang, S.C. Glotzer, S.Z.D. Cheng, Geometry Induced Sequence of Nanoscale Frank-Kasper and Quasicrystal Mesophases in Giant Surfactants, Proc. Natl. Acad. Sci. 113 (50) (2016) 14195–14200, https://doi.org/10.1073/pnas.1609422113.

[27] S. Hajiw, B. Pansu, J.-F. Sadoc, Evidence for a C14 Frank-Kasper Phase in One-Size Gold Nanoparticle Superlattices, ACS Nano 9 (8) (2015) 8116–8121, https://doi.org/10.1021/acsnano.5b02216.

[28] *Frank and Kasper phases*. Crystallography for soft matter. https://softqc.wordpress.com/frank-and-kasper-phases/ (accessed 2023-11-06).

[29] J.A. Fan, C. Wu, K. Bao, J. Bao, R. Bardhan, N.J. Halas, V.N. Manoharan, P. Nordlander, G. Shvets, F. Capasso, Self-Assembled Plasmonic Nanoparticle Clusters, Science 328 (5982) (2010) 1135–1138, https://doi.org/10.1126/science.1187949.

[30] A.P. Manuel, A. Kirkey, N. Mahdi, K. Shankar, Plexcitonics – Fundamental Principles and Optoelectronic Applications, J. Mater. Chem. C 7 (7) (2019) 1821–1853, https://doi.org/10.1039/C8TC05054F.

[31] D.S. Dovzhenko, S.V. Ryabchuk, Y.P. Rakovich, I.R. Nabiev, Light-Matter Interaction in the Strong Coupling Regime: Configurations, Conditions, and Applications, Nanoscale 10 (8) (2018) 3589–3605, https://doi.org/10.1039/C7NR06917K.

[32] F.M. Balci, S. Sarisozen, N. Polat, S. Balci, Colloidal Nanodisk Shaped Plexcitonic Nanoparticles with Large Rabi Splitting Energies, J. Phys. Chem. C 123 (43) (2019) 26571–26576, https://doi.org/10.1021/acs.jpcc.9b08834.

[33] W. Wei, F. Bai, H. Fan, Surfactant-Assisted Cooperative Self-Assembly of Nanoparticles into Active Nanostructures, iScience 11 (2019) 272–293, https://doi.org/10.1016/j.isci.2018.12.025.

[34] C. Maria Magdalane, K. Kaviyarasu, A. Raja, M.V. Arularasu, G.T. Mola, A.B. Isaev, N.A. Al-Dhabi, M.V. Arasu, B. Jeyaraj, J. Kennedy, M. Maaza, Photocatalytic Decomposition Effect of Erbium Doped Cerium Oxide Nanostructures Driven by Visible Light Irradiation: Investigation of Cytotoxicity, Antibacterial Growth Inhibition Using Catalyst, J. Photochem. Photobiol. B 185 (2018) 275–282, https://doi.org/10.1016/j.jphotobiol.2018.06.011.

[35] A.J. Rodriguez, C.D. Grinter, Z. Liu, M.R. Palomino, D.S. Senanayake, Ceria-Based Model Catalysts: Fundamental Studies on the Importance of the Metal-Ceria Interface in CO Oxidation, the Water-Gas Shift, CO 2 Hydrogenation, and Methane and Alcohol Reforming, Chem. Soc. Rev. 46 (7) (2017) 1824–1841, https://doi.org/10.1039/C6CS00863A.

[36] C. Yang, X. Yu, S. Heißler, A. Nefedov, S. Colussi, J. Llorca, A. Trovarelli, Y. Wang, C. Wöll, Surface Faceting and Reconstruction of Ceria Nanoparticles, Angew. Chem. Int. Ed. 56 (1) (2017) 375–379, https://doi.org/10.1002/anie.201609179.

[37] R. Fiorenza, L. Spitaleri, A. Gulino, S. Scirè, Ru–Pd Bimetallic Catalysts Supported on CeO2-MnOX Oxides as Efficient Systems for H2 Purification through CO Preferential Oxidation, Catalysts 8 (5) (2018) 203, https://doi.org/10.3390/catal8050203.

[38] M. Gu, W. Li, L. Jiang, X. Li, Recent Progress of Rare Earth Doped Hydroxyapatite Nanoparticles: Luminescence Properties, Synthesis and Biomedical Applications, *Acta Biomater.* 148 (2022) 22–43, https://doi.org/10.1016/j.actbio.2022.06.006.

[39] P. Jethva, M. Momin, T. Khan, A. Omri, Lanthanide-Doped Upconversion Luminescent Nanoparticles—Evolving Role in Bioimaging, Biosensing, and Drug Delivery, Materials 15 (7) (2022) 2374, https://doi.org/10.3390/ma15072374.

[40] S. Rajeshkumar, P. Naik, Synthesis and Biomedical Applications of Cerium Oxide Nanoparticles – A Review, Biotechnol. Rep. 17 (2018) 1–5, https://doi.org/10.1016/j.btre.2017.11.008.

[41] M. Auffan, J. Rose, T. Orsiere, M. De Meo, A. Thill, O. Zeyons, O. Proux, A. Masion, P. Chaurand, O. Spalla, A. Botta, M.R. Wiesner, J.-Y. Bottero, CeO2 Nanoparticles Induce DNA Damage towards Human Dermal Fibroblasts in Vitro, Nanotoxicology 3 (2) (2009) 161–171, https://doi.org/10.1080/17435390902788086.

[42] Y. Gao, K. Chen, J. Ma, F. Gao, Cerium Oxide Nanoparticles in Cancer, OncoTargets Ther. 7 (2014) 835–840, https://doi.org/10.2147/OTT.S62057.

[43] M. Nyoka, Y.E. Choonara, P. Kumar, P.P.D. Kondiah, V. Pillay, Synthesis of Cerium Oxide Nanoparticles Using Various Methods: Implications for Biomedical Applications, Nanomaterials 10 (2) (2020) 242, https://doi.org/10.3390/nano10020242.

[44] J. Wu, X. Wang, Q. Wang, Z. Lou, S. Li, Y. Zhu, L. Qin, H. Wei, Nanomaterials with Enzyme-like Characteristics (Nanozymes): Next-Generation Artificial Enzymes (II), Chem. Soc. Rev. 48 (4) (2019) 1004–1076, https://doi.org/10.1039/C8CS00457A.

[45] C. Walkey, S. Das, S. Seal, J. Erlichman, K. Heckman, L. Ghibelli, E. Traversa, F. J. McGinnis, T.W. Self, Catalytic Properties and Biomedical Applications of Cerium Oxide Nanoparticles, Environ. Sci. Nano 2 (1) (2015) 33–53, https://doi.org/10.1039/C4EN00138A.

[46] A. Dhall, W. Self, Cerium Oxide Nanoparticles: A Brief Review of Their Synthesis Methods and Biomedical Applications, Antioxidants 7 (8) (2018) 97, https://doi.org/10.3390/antiox7080097.

[47] N. Gallucci, G. Vitiello, R. Di Girolamo, P. Imbimbo, D.M. Monti, O. Tarallo, A. Vergara, I. Russo Krauss, L. Paduano, Towards the Development of Antioxidant Cerium Oxide Nanoparticles for Biomedical Applications: Controlling the Properties by Tuning Synthesis Conditions, Nanomaterials 11 (2) (2021) 542, https://doi.org/10.3390/nano11020542.

[48] N. Gallucci, M. Hmoudah, E. Martinez, A. El-Qanni, M. Di Serio, L. Paduano, G. Vitiello, V. Russo, Photodegradation of Ibuprofen Using CeO2 Nanostructured Materials: Reaction Kinetics, Modeling, and Thermodynamics, J. Environ. Chem. Eng. 10 (3) (2022) 107866, https://doi.org/10.1016/j.jece.2022.107866.

[49] M. Perfetti, N. Gallucci, I. Russo Krauss, A. Radulescu, S. Pasini, O. Holderer, G. D'Errico, G. Vitiello, G.O. Bianchetti, L. Paduano, Revealing the Aggregation Mechanism, Structure, and Internal Dynamics of Poly(Vinyl Alcohol) Microgel Prepared through Liquid-Liquid Phase Separation, Macromolecules 53 (3) (2020) 852–861, https://doi.org/10.1021/acs.macromol.9b02203.

[50] A. Luchini, D. Cavasso, A. Radulescu, G. D'Errico, L. Paduano, G. Vitiello, Structural Organization of Cardiolipin-Containing Vesicles as Models of the Bacterial Cytoplasmic Membrane, Langmuir 37 (28) (2021) 8508–8516, https://doi.org/10.1021/acs.langmuir.1c00981.

[51] N.P. Cowieson, C.J.C. Edwards-Gayle, K. Inoue, N.S. Khunti, J. Doutch, E. Williams, S. Daniels, G. Preece, N.A. Krumpa, J.P. Sutter, M.D. Tully, N.J. Terrill, R.P. Rambo, Beamline B21: High-Throughput Small-Angle X-Ray Scattering at Diamond Light Source, J. Synchrotron Radiat. 27 (5) (2020) 1438–1446, https://doi.org/10.1107/S1600577520009960.

[52] D. Pallotti, E. Orabona, S. Amoruso, P. Maddalena, S. Lettieri, Modulation of Mixed-Phase Titania Photoluminescence by Oxygen Adsorption, Appl. Phys. Lett. 105 (3) (2014) 031903, https://doi.org/10.1063/1.4891038.

[53] A. Setaro, A. Bismuto, S. Lettieri, P. Maddalena, E. Comini, S. Bianchi, C. Baratto, G. Sberveglieri, Optical Sensing of NO2 in Tin Oxide Nanowires at Sub-Ppm Level, Sens. Actuators B Chem. 130 (1) (2008) 391–395, https://doi.org/10.1016/j.snb.2007.09.015.

[54] N.A. Mahynski, S.K. Kumar, A.Z. Panagiotopoulos, Relative Stability of the FCC and HCP Polymorphs with Interacting Polymers, Soft Matter 11 (2) (2014) 280–289, https://doi.org/10.1039/C4SM02191F.

[55] I. Sanchez-Burgos, E. Sanz, C. Vega, R.J. Espinosa, Fcc vs. Hcp Competition in Colloidal Hard-Sphere Nucleation: On Their Relative Stability, Interfacial Free Energy and Nucleation Rate, Phys. Chem. Chem. Phys. 23 (35) (2021) 19611–19626, https://doi.org/10.1039/D1CP01784E.

[56] J. Luo, Z. Xie, Y.J.W. Lam, L. Cheng, H. Chen, C. Qiu, H. Sing Kwok, X. Zhan, Y. Liu, D. Zhu, B. Zhong Tang, Aggregation-Induced Emission of 1-Methyl-1,2,3,4,5-Pentaphenylsilole, Chem. Commun. (18) (2001) 1740–1741, https://doi.org/10.1039/B105159H.

[57] J. Chen, C.C.W. Law, J.W.Y. Lam, Y. Dong, S.M.F. Lo, I.D. Williams, D. Zhu, B. Z. Tang, Synthesis, Light Emission, Nanoaggregation, and Restricted Intramolecular Rotation of 1,1-Substituted 2,3,4,5-Tetraphenylsiloles, Chem. Mater. 15 (7) (2003) 1535–1546, https://doi.org/10.1021/cm021715z.

[58] Z. Zhao, H. Zhang, J.W.Y. Lam, B.Z. Tang, Aggregation-Induced Emission: New Vistas at the Aggregate Level, Angew. Chem. Int. Ed. 59 (25) (2020) 9888–9907, https://doi.org/10.1002/anie.201916729.

[59] D. Jassby, M. Wiesner, Characterization of ZnS Nanoparticle Aggregation Using Photoluminescence, Langmuir ACS J. Surf. Colloids 27 (3) (2011) 902–908, https://doi.org/10.1021/la103470r.

[60] Y.-J. Lee, T.-G. Kim, Y.-M. Sung, Lattice Distortion and Luminescence of CdSe/ZnSe Nanocrystals, Nanotechnology 17 (14) (2006) 3539, https://doi.org/10.1088/0957-4484/17/14/030.

[61] D.S. Reddy, B. Kang, S.C. Yu, K.R. Gunasekhar, K.N. Rao, P.S. Reddy, Strain, Luminescence, and Electrical Properties of Zn1−xMnxS Nanocrystalline Films Prepared on Silicon Wafers, J. Appl. Phys. 104 (1) (2008) 013532, https://doi.org/10.1063/1.2955270.

[62] N. Hildebrandt, K.D. Wegner, W.R. Algar, Luminescent Terbium Complexes: Superior Förster Resonance Energy Transfer Donors for Flexible and Sensitive Multiplexed Biosensing, Coord. Chem. Rev. 273–274 (2014) 125–138, https://doi.org/10.1016/j.ccr.2014.01.020.

[63] D. Geißler, S. Linden, K. Liermann, K.D. Wegner, L.J. Charbonnière, N. Hildebrandt, Lanthanides and Quantum Dots as Förster Resonance Energy Transfer Agents for Diagnostics and Cellular Imaging, Inorg. Chem. 53 (4) (2014) 1824–1838, https://doi.org/10.1021/ic4017883.

[64] X. Yan, Y. Cui, W. Qi, Y. Su, Y. Yang, Q. He, J. Li, Self-Assembly of Peptide-Based Colloids Containing Lipophilic Nanocrystals, Small 4 (10) (2008) 1687–1693, https://doi.org/10.1002/smll.200800960.

[65] C. Yuan, R. Liu, S. Wang, G. Han, M.-Y. Han, C. Jiang, Z. Zhang, Single Clusters of Self-Assembled Silver Nanoparticles for Surface-Enhanced Raman Scattering Sensing of a Dithiocarbamate Fungicide, J. Mater. Chem. 21 (40) (2011) 16264, https://doi.org/10.1039/c1jm12919h.

[66] *Engineered SERS Substrates with Multiscale Signal Enhancement: Nanoparticle Cluster Arrays | ACS Nano*. https://pubs.acs.org/doi/10.1021/nn800836f (accessed 2023-12-06).